

Electromechanical coupling mechanisms at a plasma-liquid interface

A. Dickenson, J. L. Walsh, M. I. Hasan*

Centre for Plasma Microbiology, Electrical and Electronics Engineering Department, University of Liverpool, Brownlow Hill, L69 3 GJ, Liverpool, UK

Abstract: The direct interaction between a non-equilibrium gas discharge and a liquid volume leads to the generation of a plasma activated liquid (PAL). This interaction induces a flow in both the gas above the liquid and within the liquid volume. The physical mechanisms behind the induced flows are complex. In this work, a two-dimensional experimentally validated numerical model was developed to determine the dominant mechanism driving the liquid flow at the plasma-liquid interface. The model followed the evolution of the plasma and the flow fields in both phases, describing a pin-water discharge configuration operating in air, which was used to treat a deionized water sample and a tap water sample. Two potential physical mechanisms were investigated, the Electrohydrodynamic (EHD) flow induced in the gas phase and the electric surface stresses across the interface. It was found that the dominant mechanism driving the liquid flow is correlated with the charge relaxation time of the liquid. For liquids with a charge relaxation time longer than the characteristic time of the plasma, such as deionized water, the liquid behaves as a dielectric and the electric surface stresses dominate the flow in the liquid phase. For liquids with a charge relaxation time shorter or in the same order of the plasma's characteristic time, such as tap water, the liquid behaves as a conductor and the EHD flow induced in the gas phase dominates the flow in the liquid phase.

1. Introduction:

Cold Atmospheric Plasmas (CAP) have been the focus of an intense research effort in recent years due to their unique ability to generate a mixture of highly reactive chemical species under ambient conditions. The number of applications where the use of CAP has been explored is growing rapidly and promising results have been obtained spanning the domains of agriculture^{1,2}, Plasma medicine³⁻⁵, and materials processing^{6,7}. In many of these applications the discharge inevitably interacts with some form of liquid, be it moisture on freshly harvested vegetables, right through to the deliberate treatment of a liquid volume to create plasma activated liquid (PAL). Using PAL offers the intriguing possibility of retaining some chemical activity initiated by the plasma for several days⁸⁻¹⁰, which is a

*Corresponding author: mihasan@liverpool.ac.uk

major advantage for most applications. Unfortunately, this advantage comes at a price, as the introduction of a plasma-water interface vastly increases the complexity of the physiochemical processes at play.

A variety of CAP sources have been used to activate liquids, these can be categorised based on whether the plasma is in direct contact with the liquid surface or not. In non-contact sources, the plasma is generated some distance away from the interface, and the reactive species generated by the plasma are carried to the interface by diffusion, convection or both ^{11,12}. Such sources include Surface Barrier Discharges (SBD) ^{11,13}, gliding arc discharges ^{14,15}, and plasma jets where the plasma terminates before arriving to the interface ^{12,16}. In direct-contact sources, on the other hand, the plasma physically contacts the liquid surface, creating a complex gas-water-plasma interface. This leads to a higher dose of short-lived species such as ions and radicals reaching the water, and thus a higher activation in a shorter period of time ^{17,18}. Examples of such discharge configurations include pin-water discharges ^{19,20}, water film DBD ²¹, and some configurations of plasma jets ²².

Whether PAL is generated using a contact or a non-contact source, there is potential for the plasma treatment to induce a flow in the liquid phase ²³. For non-contact sources this flow can be explained by the mechanical coupling between the gas phase flow and liquid surface, where the gas flow can be that from a plasma jet, or from the Electrohydrodynamic (EHD) forces in an SBD. This gas flow sets the liquid's free surface in motion, leading to a flow in the bulk liquid due to shear stresses, which was reported in numerical and experimental studies^{24,25}. For contact sources, however, there are multiple processes at play. One of which is the mechanical coupling between the gas flow, generated by Electrohydrodynamic (EHD) forces and the liquid phase ^{26,27}. The mechanical coupling typically leads to the formation of a dip at the interface as it pushes the liquid downwards ^{12,24}. Another process at play is the electric coupling, represented by electric surface stresses that can drive a flow in the bulk liquid phase, which typically leads to the formation of a cone or a hump at the interface by pulling the surface upwards ^{20,28}. Flows driven by electric surface stresses are the

main concept behind electrosprays and EHD atomisers^{29,30}, where a strong electric field is applied to a liquid, causing its surface to form a Taylor cone which breaks into a jet of droplets. Considering its importance for many applications, this process has been studied extensively experimentally and numerically³¹⁻³⁴. In the context of plasma-liquid interaction, previous works have focused on the pre-breakdown stage of the discharge and the initial deformation of the liquid before the discharge ignites^{20,28,35}, where it has been reported that the surface of the water forms a hump for values of applied voltage below the critical stability limit, for higher voltages a Taylor cone was observed at the interface²⁵.

Few quantitative studies of the complex interplay between the mechanical and the electrical processes have been performed, despite its importance for the transport of reactive species across the liquid interface. For example, Mitsugi *et al* have studied the plasma jet-induced flow in a water sample using Particle Image Velocimetry (PIV)³⁶, where they reported that the velocity of the bulk liquid is of the order of $10 \text{ mm}\cdot\text{s}^{-1}$ and that surface pressure waves were driving the surface flow in the radial direction. Lai *et al* used PIV and Shadowgraphy imaging to study flow instabilities at a plasma-liquid interface³⁷, where their analysis indicated the presence of a Kelvin-Helmholtz perturbation that causes sharp velocity shear, inducing vortices in the shearing layers.

The objective of this work was to quantify the influence of these processes in driving the liquid flow in Plasma Activated Water (PAW) reactors where the plasma contacts the liquid's interface. This was achieved by implementing a numerical model to describe a pin-water discharge configuration operating in air. The model was experimentally-validated and was able to capture the EHD induced flow in the gas phase, and the electric surface stresses exerted by the plasma's sheath on the interface. The remainder of this manuscript is organised as follows, section 2 describes the experimental setup used to validate the numerical model, which is described in section 3. Section 4 presents the experimental and numerical results of the study and a conclusion is provided in section 5.

2. Experimental setup

The experimental setup employed in this study was used to generate plasma in direct contact with a liquid surface and facilitate the measurement of the velocity fields in both the gas and liquid phases using Particle Image Velocimetry (PIV).

2.1 Electrode configuration and power source

A pin-water discharge configuration operating in air was setup to expose a 125 ml volume of water. A 2 mm diameter Tungsten pin was mounted vertically 5 mm above the water surface. The pin was connected to a custom-made high voltage power supply, capable of providing a sinusoidal signal in the kV range at 10s of kHz frequency range. The ground electrode was a copper wire inserted into the liquid volume at the container wall, approximately 35 mm from the discharge contact point. The discharge voltage and current were measured using a Tektronix DPO 5054 oscilloscope and Pearson 2877 current probe. The dissipated power was calculated by averaging the product of the voltage and current over 450 cycles in real-time on the oscilloscope.

Two samples of water were considered in this study, a deionized sample with a conductivity of $2 \mu\text{S cm}^{-1}$, measured using Hanna Instruments HI 1285-5 multiparameter probe, and a tap sample with a conductivity of $300 \mu\text{S cm}^{-1}$. For each test a 125 ml volume of liquid was pipetted into a plastic container measuring 50 x 50 x 75 mm in width x length x depth. All samples were plasma treated at a constant power of approximately 15 W. To achieve a dissipated power of 15 W, peak to peak voltages of 11 kV and 8 kV were required for the deionized and tap water samples, respectively. During operation it was apparent that plasma formation caused distortion of the applied voltage waveform due to loading of the high voltage transformer. To ensure comparable behaviour between the model and the experiment the recorded voltage waveforms were used as inputs to the model. A schematic diagram of the discharge configuration is shown in figure 1(a).

2.2 Particle Image Velocimetry (PIV) measurements

While the discharge was in operation PIV measurements were performed to obtain the velocity vector fields in both the gas and the liquid phase. The full operating principle of the PIV technique is described elsewhere³⁸, here it is explained in brief. The entire experimental setup was placed within a large sealed chamber, measuring 1 x 1 x 1.5 m in height x width x length. The chamber had two windows, one enabled a laser light sheet to be projected across the experimental setup, and the other enabled an observation to be made perpendicular to the laser sheet, as shown in figure 1(b). The chamber was filled with oil droplets, with a nominal diameter of 1 μm , to scatter the laser light. To obtain velocity measurements in the liquid volume, melamine particles with a nominal diameter of 10 μm were used. When the discharge was in operation, a 30 mJ pulsed Nd:YLF laser operating with a pulse duration of 100 ns at 527 nm, was used to produce two consecutive laser sheets with a controllable time delay. Simultaneously, a high-speed camera (Phantom Micro 340) was used to capture a single laser pulse in each frame. Using a cross-correlation procedure the 2D velocity vector field was calculated for each pair of camera frames³⁹. Considering that the Stokes number of the seeding particles for both the gas and liquid phase measurements was less than 0.1, the velocity of the particle seeds was within 1% of the background flow^{40,41}.

Considering the significant difference between the liquid velocity and gas velocity, the time delay between the laser sheets was set to 50 μs for the gas phase and set to 5200 μs for the liquid phase at a laser pulse repetition frequency of 400 Hz and 200 Hz respectively. Consequently, it was not possible to obtain gas and liquid velocity measurements simultaneously. For each experimental run, a total of 500 frames were captured and averaged to calculate the time-averaged velocity field after a given time, corresponding to 1.25 s for gas phase and 2.5 s for the liquid phase. Due to the scattering of laser light from the liquid surface, the PIV processing interrogation area was set 0.5 mm below the interface when calculating the liquid velocity field. For the same reason, in the gas phase the interrogation was set 0.5 mm above the interface, as labelled in figure 1(a). It was not possible to perform PIV measurements for the deionized liquid sample due to severe surface perturbation

resulting from plasma interaction. A video showing the unstable surface for the deionized sample case can be found in the supplementary materials.

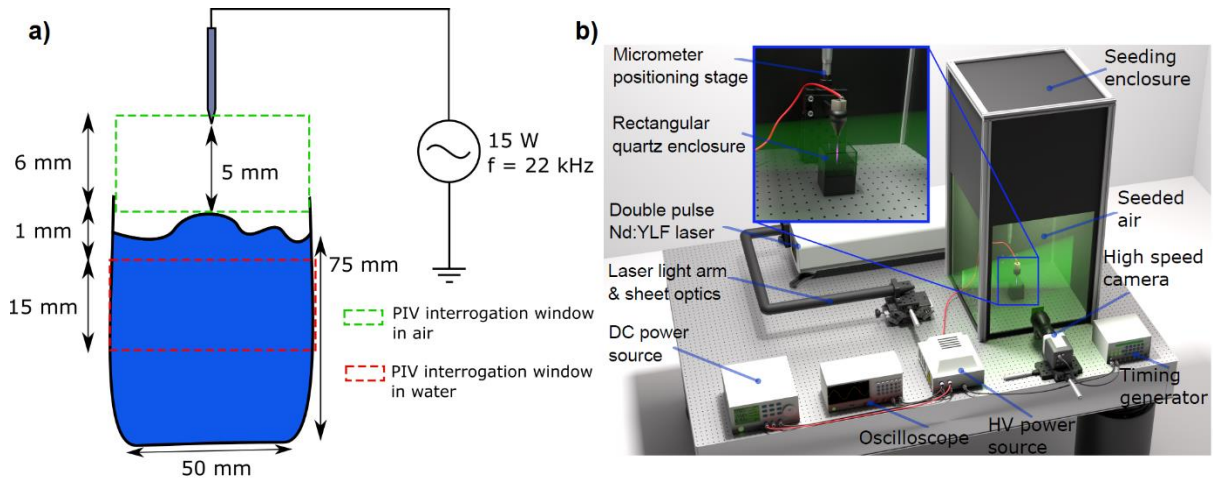


Figure 1: a) A schematic of the discharge configuration showing the dimensions and the position of PIV interrogation areas with respect to the discharge, b) the PIV experimental set up.

3. Numerical model:

A two-dimensional time dependent axisymmetric computational model was used in this study, consisting of two components: a mechanical component for capturing the fluid flow in both the gas and liquid phases, and an electric component for capturing the plasma dynamics. The model was designed to represent the experimental conditions as close as possible; therefore, all the parameters of the model such as the geometry, and the liquid sample's conductivity were chosen to match those used in the experiments. The inputs to the model were the voltage waveforms from the experiments. The outputs of the model were the velocity fields in both phases, in addition to the electric field and the species densities in the plasma. The computed velocity fields were compared to those measured using PIV in order to validate the computational model. Despite the difference in the geometry between the experimental setup and the axisymmetric nature of the model, such a difference will not have a significant influence on the comparison given that the plasma-liquid contact area is much smaller than the surface area of the gas liquid interface and is situated in the

center of the container well away from the walls. The domain of the computational model and the relation between its components is shown in figure 2.

Initially, the mechanical component of the model was run to compute the induced flow by the electric field just before breakdown, in addition to the initial surface structure and induced surface charge on the surface. Those parameters served as the initial conditions for the electric component, which was solved for the time-averaged EHD forces fields and electric surface stresses at the interface, which were subsequently used as inputs to the mechanical component, in order to solve for the plasma induced flow.

In formulating the model, it was assumed that the plasma treatment time of the water samples is not long enough to alter their conductivity. This assumption was justified as the model followed the first few seconds of the plasma treatment. Experimentally it was shown that a significant change in the conductivity of the treated water occurs on the order of minutes of treatment ⁴².

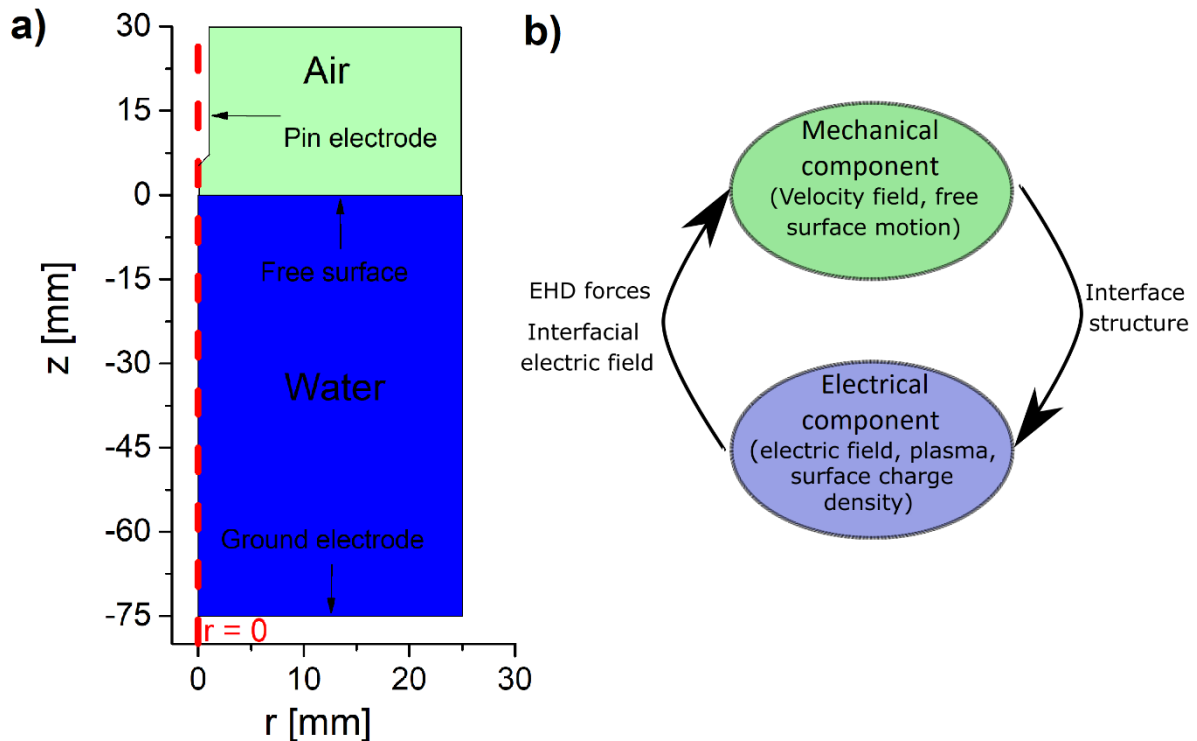


Figure 2: Schematic showing: a) the computational domain of the model, and b) the coupling between the two components of the model and the variables exchanged between them.

3.1 The mechanical component

The mechanical component of the model solved for the flow field in both phases, the plasma-free electric field, the interfacial surface charge from the liquid phase, and the free surface (the interface) deformation. For the fluid flow the mass continuity equation and Navier-Stokes equation were solved in both phases, as given by equations 1 and 2 respectively.

$$\frac{\partial \rho}{\partial t} + \nabla \cdot (\rho \vec{u}) = 0 \quad (1)$$

$$\rho \frac{\partial \vec{u}}{\partial t} + \rho (\vec{u} \cdot \nabla) \vec{u} = \nabla \cdot (-pI + \bar{\tau}) - \rho \vec{g} + \vec{F}_{EHD} \quad (2)$$

In equations 1 and 2, ρ is the fluids mass density ($\text{kg}\cdot\text{m}^{-3}$), which was calculated by the model in air assuming the ideal gas law, and was set to 998 in water meaning that water was treated as incompressible fluid, \vec{u} is the velocity field in both phases ($\text{m}\cdot\text{s}^{-1}$), p is the pressure (Pa) which was obtained from the ideal gas law in the gas phase, and was computed as a variable in the liquid phase, I is the identity matrix, $\bar{\tau}$ is the stress tensor given in equation 3, \vec{g} is gravity's acceleration ($\text{m}\cdot\text{s}^{-2}$). The gravity acceleration term was only applied to the liquid phase. Lastly, F_{EHD} is the time-averaged force density due to the EHD forces exerted by the charged species in plasma in the gas phase ($\text{N}\cdot\text{m}^{-3}$). This term was set to 0 when the mechanical component was initially solved. To close the system, an explicit form of the stress tensor is needed. The stress tensor is given by equation 3.

$$\bar{\tau} = \zeta (\nabla \vec{u} + (\nabla \vec{u})^T) - \frac{2}{3} \zeta (\nabla \cdot \vec{u}) I + \varepsilon \vec{E} \vec{E} - \frac{1}{2} \varepsilon (\vec{E} \cdot \vec{E}) I \quad (3)$$

In equation 3, ζ is the dynamic viscosity of the fluid ($\text{Pa}\cdot\text{s}$), which was set to 1.81×10^{-5} and 1×10^{-3} for air and water respectively, ε is the electric permittivity of the medium which was set to ε_0 ($\text{F}\cdot\text{m}^{-1}$) for air and $81\varepsilon_0$ for water, \vec{E} is the electric field ($\text{V}\cdot\text{m}^{-1}$) which was determined from equation 4.

Equation 3 has two types of stresses, the first is the viscous stress represented by the first two terms, the second is the electric field stress represented by Maxwell's stress tensor appearing as the

last two terms in equation 3⁴³. Considering that F_{EHD} accounted for the electric forces in the gas phase, Maxwell stress tensor was accounted for in the liquid phase only. To calculate the electric field, the Laplace equation was solved for the electric potential everywhere in the computational domain, as given in equation 4.

$$\nabla \cdot (-\varepsilon \nabla V) = 0 \quad (4)$$

In equation 4, V is the electric potential (V), and the electric field was computed from the potential by $\vec{E} = -\nabla V$. It should be noted that the electric field was also solved in the mechanical component to account for any field-induced deformation of the interface prior to breakdown. When an electric field is applied in the liquid phase, where positive and negative ions exist, counter-ions are attracted from the bulk to the interface to shield the electric field, forming surface charge. To compute that surface charge, equation 5 was solved. The surface charge density on the interface was treated as a boundary condition when solving equation 4.

$$\frac{\partial \sigma}{\partial t} = \hat{n} \cdot (q_e \mu n_i \vec{E}) \quad (5)$$

In equation 5, σ is the surface charge density ($C \cdot m^{-2}$), \hat{n} is the normal unit vector on the surface, μ is the ionic mobility in water ($m^2 \cdot V^{-1} \cdot s^{-1}$), n_i is the initial ion density in the liquid (m^{-3}). Considering that the ions mobility and density appear as a product in the equation, the value of their product μn_i was set to match the experimental conductivity for the investigated water samples.

The imposed boundary conditions on the interface enforced the continuity of the flow field, as given in equations 6a to 6c.

$$\hat{n} \cdot \vec{u} = 0 \quad (6a)$$

$$[\vec{u}] = 0 \quad (6b)$$

$$\hat{n} \cdot [\vec{\tau}] = \gamma(\nabla \cdot \hat{n})\hat{n} - \nabla \gamma - \hat{n} \cdot [\varepsilon \vec{E} \vec{E}] - \frac{1}{2}[\varepsilon \vec{E} \cdot \vec{E}]\hat{n} \quad (6c)$$

In equations 6a-6c, the “[]” brackets represent the “jump” across the surface from the liquid phase into the gas phase. Equation 6a is a no-permeability condition, equation 6b is a no-slip condition

(meaning the velocity components are continuous along the interface), and equation 6c states that the jump in the normal stress is equal to surface forces. The first two terms in the right-hand side of equation 6c represent surface tension forces, where γ is the surface tension coefficient ($\text{N}\cdot\text{m}^{-1}$), which was set equal to 0.073 for the air-water interface. Revisiting the electric field stress given in equation 3; considering that the width of a typical electric double layer at the air-water interface is in the nm range ²³, i.e. much smaller than the dimensions of the model, it was possible to treat the electric stresses as a surface force instead of a volumetric force as described by equation 3.

Consequently, the last two terms in the right-hand side of equation 6c represent the electric “surface” stress, and the “volumetric” electric stress is no longer accounted for in equation 3.

Since equations 6a-6c allow for a non-zero velocity to exist on the interface, this means that the interface may deform due to its flow velocity. To capture the deformation of the interface the Arbitrary Lagrangian-Eulerian (ALE) method was implemented ⁴⁴. This method splits the coordinates used in the model into spatial coordinates (r,z) and reference coordinates (R,Z), as the location of the interface evolved, a smoothing equation was solved to map the reference coordinates to the spatial coordinates, which is given by equation 7.

$$\frac{\partial}{\partial R^2} \frac{\partial r}{\partial t} + \frac{\partial}{\partial Z^2} \frac{\partial z}{\partial t} = 0 \quad (7)$$

In equation 7, r and z (mm) are the spatial coordinates (the instantaneous coordinates as the simulation was solved), while R and Z (mm) are the reference coordinates (the initial coordinates at the start time of the model). Equation 7 was connected to equations 6a-6c through equations 8a and 8b, where u_{surf} and w_{surf} are the velocity components in the r and z directions respectively ($\text{m}\cdot\text{s}^{-1}$).

$$\frac{\partial R}{\partial t} = u_{surf} \quad (8a)$$

$$\frac{\partial Z}{\partial t} = w_{surf} \quad (8b)$$

For the remaining boundaries, a symmetry boundary condition for all variables solved for was imposed on the boundary $r = 0$. For the boundaries at $z = 30$ mm and $r = 25$ mm, the normal viscous

stresses and electric fields were set to 0 which represented an open boundary. A no slip boundary condition was imposed on the pin's surface for the fluid flow, and a time varying potential was imposed for solving equation 4. For boundaries making container of the water sample, a no slip boundary condition was imposed, and the ground electrode was imposed at the bottom boundary.

3.2 The electric component

The electric component of the model accounted for the generation of the plasma and how it affected the electric field. The electric component was based on a plasma fluid model consisting of a system of mass continuity equations following the evolution of 6 species in space and time and 13 reactions associated with them. The species were e^- , N_2^+ , O_2^+ , O_2^- , O_2 and N_2 and the reactions included in the model and their rate coefficients are given in table 1. For every species equations 9a and 9b were solved. In addition to one additional conservation equation for the electron energy density, as given by equation 10.

$$\frac{\partial n_k}{\partial t} + \nabla \cdot \vec{\Gamma}_k = \sum_l k_{lj} n_j n_l \quad (9a)$$

$$\vec{\Gamma}_k = \mu_k n_k \vec{E} - D_k \nabla n_k \quad (9b)$$

$$\frac{\partial n_{en}}{\partial t} + \nabla \cdot (-\mu_{en} n_{en} \vec{E} - D_{en} \nabla n_{en}) = \sum_l \theta_l k_{lj} n_j n_l - \vec{\Gamma}_e \cdot \vec{E} \quad (10)$$

In equations 9-10, n_k is the density of the k^{th} species (m^{-3}), $\vec{\Gamma}_k$ is the flux of the k^{th} species ($\text{m}^{-2} \cdot \text{s}^{-1}$), k_{ij} is the two-body reaction rate coefficient ($\text{m}^3 \cdot \text{s}^{-1}$), μ_k is the mobility of the k^{th} species ($\text{m}^2 \cdot \text{V}^{-1} \cdot \text{s}^{-1}$), D_k is the diffusion coefficient of the k^{th} species ($\text{m}^2 \cdot \text{s}^{-1}$), n_{en} is the electron energy density ($\text{eV} \cdot \text{m}^{-3}$), μ_{en} and D_{en} are the mobility and the diffusion coefficients respectively for the electron energy density, and θ_l is the electron's energy cost of the l^{th} reaction (eV).

The transport coefficient of ions and neutrals, namely the mobility and the diffusion coefficient, were set equal to those in other work ⁴⁵. The mobilities of the neutrals were set to 0. For electrons, the transport coefficients, μ_{en} and D_{en} were all calculated by BOLSIG+ ⁴⁷.

Table 1. The list of reactions included in the electric component of the model.

Rxn No	Reaction formula	Reaction coefficient	Energy cost	Ref
R1	$e + N_2 \rightarrow e + N_2$	$f(\epsilon_{avg})^b$	$0.3(T_e - T_g)$	[45,46]
R2	$e + O_2 \rightarrow e + O_2$	$f(\epsilon_{avg})^b$	$0.26(T_e - T_g)$	[45,46]
R3	$e + N_2 \rightarrow 2e + N_2^+$	$1 \times 10^{-16} \epsilon_{avg}^{1.9} e^{(-14.6/\epsilon_{avg})}$	15.58	[45,46]
R4	$e + O_2 \rightarrow 2e + O_2^+$	$9.54 \times 10^{-12} \epsilon_{avg}^{-1.05} e^{(-55.6/\epsilon_{avg})}$	12.07	[45,46]
R5	$e + O_2 \rightarrow O_2^-$	$9.72 \times 10^{-15} \epsilon_{avg}^{-1.62} e^{(-14.2/\epsilon_{avg})} \epsilon_{avg} > 1.13$ $2.78 \times 10^{-20} \epsilon_{avg} < 1.13$		[45,46]
R6	$e + N_2 + O_2 \rightarrow N_2 + O_2^-$	$1.1 \times 10^{-43} (T_g/T_e)^2 e^{(-70/T_g)} e^{(1500(T_e - T_g)/(T_e T_g))}$		[45,46]
R7	$e + 2O_2 \rightarrow O_2 + O_2^-$	$1.4 \times 10^{-41} (T_g/T_e) e^{(-600/T_g)} e^{(700(T_e - T_g)/(T_e T_g))}$		[45,46]
R8	$M + e + N_2^+ \rightarrow M + N_2$	$3.12 \times 10^{-35}/T_e$		[45,46]
R9	$N_2 + O_2^- \rightarrow e + O_2 + N_2$	$1.9 \times 10^{-18} (T_g/300)^{0.5} e^{(-4990/T_g)}$		[45,46]
R10	$O_2 + O_2^- \rightarrow e + O_2 + O_2$	$2.7 \times 10^{-16} (T_g/300)^{0.5} e^{(-5590/T_g)}$		[45,46]
R11	$O_2 + N_2^+ \rightarrow O_2^+ + N_2$	5×10^{-17}		[45,46]
R12	$O_2^- + N_2^+ \rightarrow O_2 + N_2$	$2 \times 10^{-13} (300/T_g)^{0.5}$		[45,46]
R13	$O_2^- + O_2^+ \rightarrow 2 O_2$	$2 \times 10^{-13} (300/T_g)^{0.5}$		[45,46]

^a ϵ_{avg} : Mean electron energy (eV), $T_e = 2q_e \epsilon_{avg} / (3k_B)$, where k_B is Boltzmann constant, T_g is the gas temperature (K), set to room temperature.

^b $f(\epsilon_{avg})$ indicates a rate coefficient that is calculated from BOSIG+

Since the plasma alters the electric field, equations 4 and 5 were updated with a plasma term to become equations 11 and 12.

$$\nabla \cdot (-\epsilon \nabla V) = \rho_v \quad (11)$$

$$\frac{\partial \sigma}{\partial t} = \hat{n} \cdot (q_e \mu n_i \vec{E}) + q_e \hat{n} \cdot (\vec{\Gamma}_{N_2^+} + \vec{\Gamma}_{O_2^+} - \vec{\Gamma}_{O_2^-} - \vec{\Gamma}_e) \quad (12)$$

The term on the right-hand side of equation 11 is the space charge density of the plasma ($C \cdot m^{-3}$), while the second term on the right-hand side of equation 12 is the net charge flux to the interface from the plasma.

While the electric component is solved, the instantaneous EHD forces and the instantaneous electric surface stresses were integrated in time ²⁷. After the electric component is finished, the time-integrated quantities were divided by the period of the waveform, thus giving the time-averaged EHD forces and the time-averaged electric surface stresses, as given in equations 13 and 14. Both terms are subsequently used as input to the mechanical component to account for the plasma-induced flow.

$$\vec{F}_{EHD} = \frac{1}{T} \int_0^T \rho_v \vec{E} dt \quad (13)$$

$$\vec{F}_E = \frac{1}{T} \int_0^T \left(\hat{n} \cdot [\varepsilon \vec{E} \vec{E}] + \frac{1}{2} \varepsilon [\varepsilon \vec{E} \cdot \vec{E}] \hat{n} \right) dt \quad (14)$$

In equations 13 and 14, T is the period of the waveform (s) and \vec{F}_E is the time-average surface electric surface stress pressure ($\text{N}\cdot\text{m}^{-2}$). After these variables were evaluated, they were introduced in equations 2 and 6c in the mechanical component of the model. This approach is applicable as long as the deformation of the surface during a single period is negligible.

All the plasma parameters were solved only in the gas phase. A symmetry boundary condition was imposed at $r = 0$ boundary for all variables solved for. For the outer boundaries of the gas phase, a continuity condition was imposed. For the boundary defining the pin electrode, a wall loss condition was imposed, which means all the diffusive flux to the wall is lost, in addition to electric-field driven flux when it is directed toward the electrode.

4. Results and discussion:

Initially, the mechanical component of the model was run until the surface arrived to its steady state structure. Then the electric component was run for one period of the applied waveform, and the mechanical component was subsequently run (taking the plasma effects into account) until reaching a steady state flow pattern, which took few seconds of solution time. The time-averaged power

dissipated at the pin electrode as calculated by the model was 10 W for the deionized sample case and 9 W for the tap sample case.

4.1 Pre-breakdown flow

At the instant prior to breakdown, the applied electric field was strong enough to cause a small “hump” to form on the interface. For the applied voltages and the pin-interface distance used in experiments, the system was under the critical stability limit for behaving as an electric spray, thus no jetting was observed experimentally, which was consistent with the model.

To form the hump on the surface, the flow in the liquid phase was in a direction that pumped water against gravity. This can be seen from figure 3, which shows the liquids flow direction in figure 3a, and the axial velocity component in the liquid phase in figure 3b.

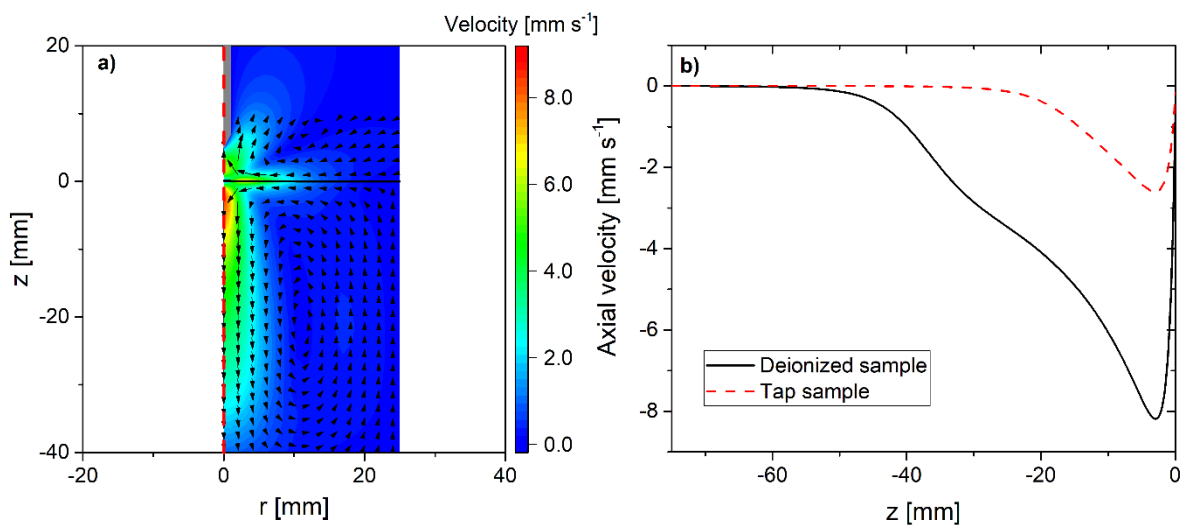


Figure 3: a) Computed flow field in both phases prior to breakdown for the deionized sample, b) the axial velocity along the symmetry axis in the liquid phase, the point $z = 0$ represents the interface.

Figure 3a shows that the direction of the water flow was from the bulk to the interface at the outer boundary of the container, then parallel to the surface to form the hump at the symmetry axis, and then back into the bulk. The formation of the hump caused the hydrostatic pressure to increase locally at the symmetry axis, which created a pressure gradient that drove the liquid flow downwards at the symmetry axis, as indicated in figure 3a. The flow of the liquid at the interface

dragged the gas, causing it to be sucked toward the symmetry axis, where the build-up of the pressure created a stream in the positive z direction as can be seen close to the pin electrode.

To quantify the flow field shown in figure 3a, figure 3b shows the axial velocity component in the liquid phase. The velocity at the surface is zero as the stagnation pressure is developed in the gas side of the interface. Moving down in the liquid, the velocity was directed toward the bottom of the container and peaked at 8 and 2.1 mm·s⁻¹ for the deionized and tap water samples, respectively. The difference in the peak velocities stemmed from using different amplitudes to drive the discharge at the same operating power.

4.2 Plasma's ignition and discharge behaviour

The behaviour of the discharge in a pin-water configuration has been widely studied and the findings in this study are in line with the past findings. The discharge was observed to ignite in the positive cycle of the applied voltage, originating at the pin electrode, where the electric field had its maximum value due to the sharp geometry at the pin's tip. A plasma cloud formed and subsequently propagated in the gap between the pin electrode and the interface as a streamer, forming a conductive plasma channel between the pin electrode and the liquid. The two-dimensional profile of the plasma channel as it formed and propagated is shown in figures 4a and 4b. The model showed that the estimated propagation velocity of the streamer was approximately 15 km·s⁻¹, and the radius of the streamer was slightly above 1 mm. Both parameters are consistent with experimental parameters reported for similar configurations^{48–50}.

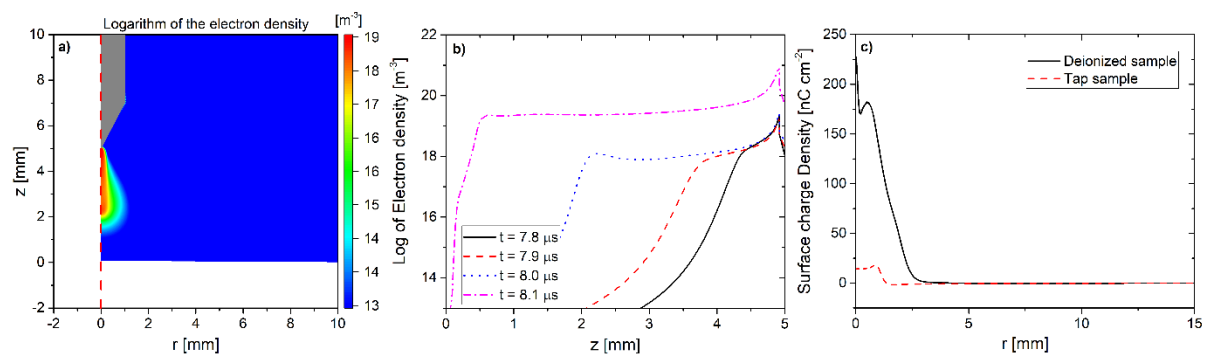


Figure 4: a) Two-dimensional colour map of the logarithm of the electron density at 8 μs for the deionized sample case, b) the logarithm of the electron density along the symmetry axis at different times for the deionized sample case, and c) the surface charge density on the interface for the deionized sample and for the tap samples at 0.5 μs after the streamer arrival to the surface.

Figure 4b also shows that as the plasma channel approaches the interface, the discharge mode transitions from a streamer-like mode into a glow-like mode, where a plasma is ignited between two conductors, leading the electron density to increase throughout the plasma channel reaching electron density of 10^{19} to 10^{20} m^{-3} , which is consistent with experimental reports on similar discharges⁴⁸.

As soon as the plasma channel was established, its interaction with the interface varied between the two investigated cases. For the deionized sample, the plasma expanded along the interface as a surface streamer, creating a branched plasma channel parallel to the surface and thus increasing the contact area. For the more conductive tap water sample, however, this effect was less profound. For both investigated cases the area of the plasma-water interface was less than 1% of the total surface area of the air-water interface, thus supporting the assumption that the influence of the difference in the geometry between the model and the experimental setup on the results was minimal.

The difference in the behaviour at the interface can be explained in terms of the conductivity of the liquid samples. As stated in section 2, the conductivity of the deionized sample was $2 \mu\text{S cm}^{-1}$ while that of the tap sample was $300 \mu\text{S cm}^{-1}$. Critically, the conductivity of the liquid controls affects its charge relaxation time, which defines the characteristic time required for the liquid to shield an external electric field. For an ideal dielectric the relaxation time is infinity as dielectrics do not shield external electric field, instead they polarize. While the relaxation time of a perfect conductor is zero. The charge relaxation times were calculated to be approximately 3.6 μs for the deionized sample and 24 ns for the tap sample.

The plasma's propagation along the water's surface occurred on a tens of nanoseconds timescale. Consequently, the surface discharge behaved like a dielectric Barrier Discharge (DBD) in the deionized sample case, where the plasma deposits surface charge on the interface, leading to a weakened electric field and causing a further radial spread along the surface. In contrast, when a tap water sample was used the plasma's propagation time was comparable to that of the charge relaxation time of the sample, thus the deposited surface charge started to decay as soon as it was deposited on the interface, making the discharge behave as a hybrid between a DBD and a glow discharge.

Figure 4c shows the surface charge density for both cases 0.5 μs after the streamer arrived at the interface. As can be seen, the deposited surface charge for the deionized sample is an order of magnitude higher than that of the tap sample. Another observation is that the surface charge distribution in the tap sample case is narrower than that in the deionized case. This is because of surface charge neutralisation, which weakened the radial propagation of the discharge.

4.3 The EHD force fields

The time-averaged EHD force field for both investigated cases showed a similar structure with different amplitudes. The radial and the axial force fields are shown in figure 5, where it can be seen that the maximum values of the force fields coincided with the positions of the plasma sheath. Namely, the tip of the pin electrode, the contact area between the plasma and the liquid, and in some cases, the radial sheath of the plasma channel. This affiliation can be explained by equation 13, as the plasma sheaths are the only regions where a non-zero charge density exist and as a result a strong electric field exists. Therefore, they are the only regions where the EHD forces are exerted.

Focusing on the radial force, figures 5a and 5b show that the maximum values of the force, directed radially inward and outward, are at the tip of the pin electrode. This is a consequence of the difference in the widths of the sheaths during the positive and the negative cycles of the waveform. During the positive cycle, the plasma channel was at a lower potential than the electrode, therefore

the electric field was directed radially outward, and the direction of the radial force was radially outward as a result. During the negative cycle, the plasma channel had a higher potential than the pin electrode and the direction of the radial force was radially inward. Considering that streamer propagation occurred in the positive cycle, the negative cycle started at a higher plasma density than the positive cycle, which led to a shorter Debye length and a narrower sheath, thus explaining why the time-averaged radial force is negative on the surface of the pin electrode.

The other region of interest in the computational domain is the contact area between the plasma and the liquid, where the time-averaged radial force has a local maximum in the radially outward direction for both samples. This force was exerted during the positive cycle where the plasma potential was higher than its surrounding, which meant that the electric field was in the radially outward direction. During the negative cycle the electric field changed its direction, however, because the plasma density was low at the contact area, the difference between the plasma potential and its surroundings was low, which led to a weak electric field. Consequently, the positive cycle behaviour dominated the time-averaged EHD force in the contact area at the plasma-liquid interface.

The main difference between figures 5a and 5b is the presence of a stronger radial force at the side sheath of the plasma channel in figure 5a compared to 5b. As explained in section 4.2, the liquid in the deionized sample (figure 5a) behaved as a lossy dielectric. This meant that the surface charge accumulation on the interface weakened the electric field in the sheath at the contact area, thus the plasma potential was primarily influenced by the pin electrode. Indeed, the variation of the plasma potential across the plasma channel did not deviate significantly from the pin electrode's potential at any given time. For the tap sample (figure 5b), the liquid behaved as a conductor with a finite conductivity, which meant that the ground electrode submerged in the water influenced the plasma potential, such that the plasma potential in the tap sample case was lower than in the deionized

sample case. This led to a weaker radial electric field and a lower time-averaged radial force at the side sheath of the plasma channel.

The time-averaged axial force for the deionized and tap water samples are shown in figures 5c and 5d, respectively. Similar to the radial force, the maximum values of the axial force, whether it is upwards or downwards, exist at the tip of the pin electrode. The positive cycle contributed to the downward force while the negative cycle contributed to the upward force. For the same reasons explained earlier, the contribution of the negative cycle extended over a smaller region than that of the positive cycle, leading to the force structure observed in figures 5c and 5d.

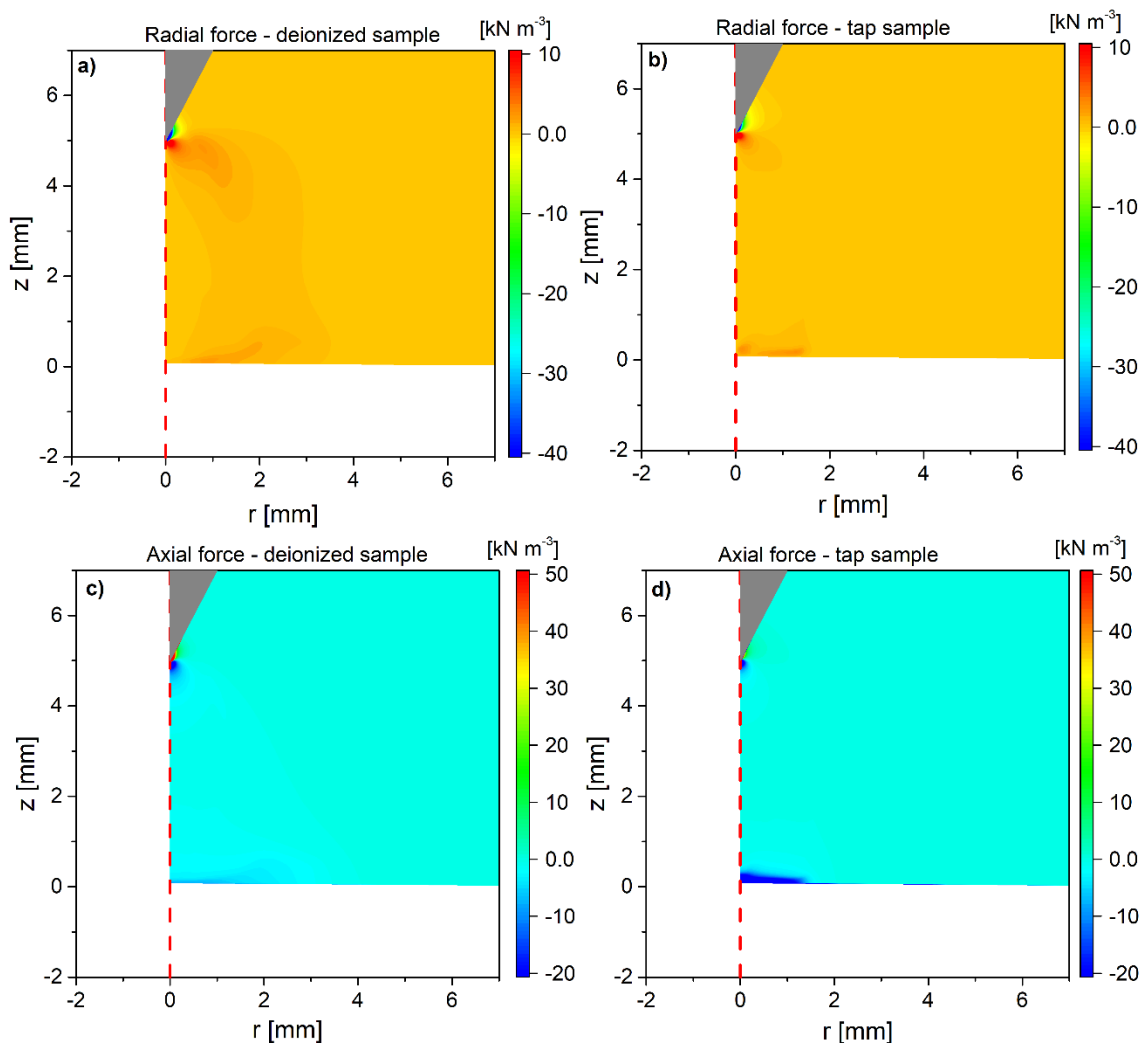


Figure 5: A two-dimensional colour map of a) the radial force density for the deionized sample, b) the radial force density for the tap sample, c) the axial force density for the deionized sample, and d) the axial force density for the tap sample. Panels a and b have the same scale while panels c and d have the same scale.

The sheath at the plasma-liquid contact area shows a significant difference between figures 5c and 5d, where there is a strong force component in the tap sample case but not in the deionized sample case. The absence of the strong force in the deionized sample case can be attributed to the accumulation of surface charge on the interface, which attenuated the axial electric field in the sheath leading to a weaker axial force. The high conductivity of the tap sample meant that significant charge accumulation could not occur on the surface, which allowed for a strong electric field to exist over longer periods of time, which contributed to the time-averaged EHD force.

Despite it not being obvious in figure 5, it should be noted that non-zero time-averaged force components exist in the plasma channel. The origin of this time-averaged force was the instantaneous force exerted by the streamer head as it propagated in the gap between the pin electrode and the liquid surface. As soon as a plasma channel was established in the gap, the instantaneous force dropped to zero as the plasma channel was charge neutral. The time-averaged force components in the plasma channel were fairly uniform, where the axial component had approximate values of $400 \text{ N}\cdot\text{m}^{-3}$ and $1800 \text{ N}\cdot\text{m}^{-3}$ for the tap sample and the deionized sample respectively in the downward direction. For the radial component the approximate values were $20 \text{ N}\cdot\text{m}^{-3}$ and $80 \text{ N}\cdot\text{m}^{-3}$ at a radius of 0.2 mm in the outward direction for the tap and deionized samples, respectively. The higher values obtained for the deionized sample can be attributed to the higher voltage needed to drive the discharge for the deionized case.

4.4 Electric surface stresses

While the electric component of the model was integrated in time, the electric surface stresses across the interface were integrated in time. The time-averaged electric surface stresses across the interface are shown in figure 6, which indicates that the electric surface stresses in the deionized

sample case were an order of magnitude higher than those for the tap sample case. It also shows that the direction of the electric surface stresses for the deionized sample was opposite to that of the tap sample. Lastly, the electric surface stresses in the deionized sample case extended over a larger area than that of the tap sample case.

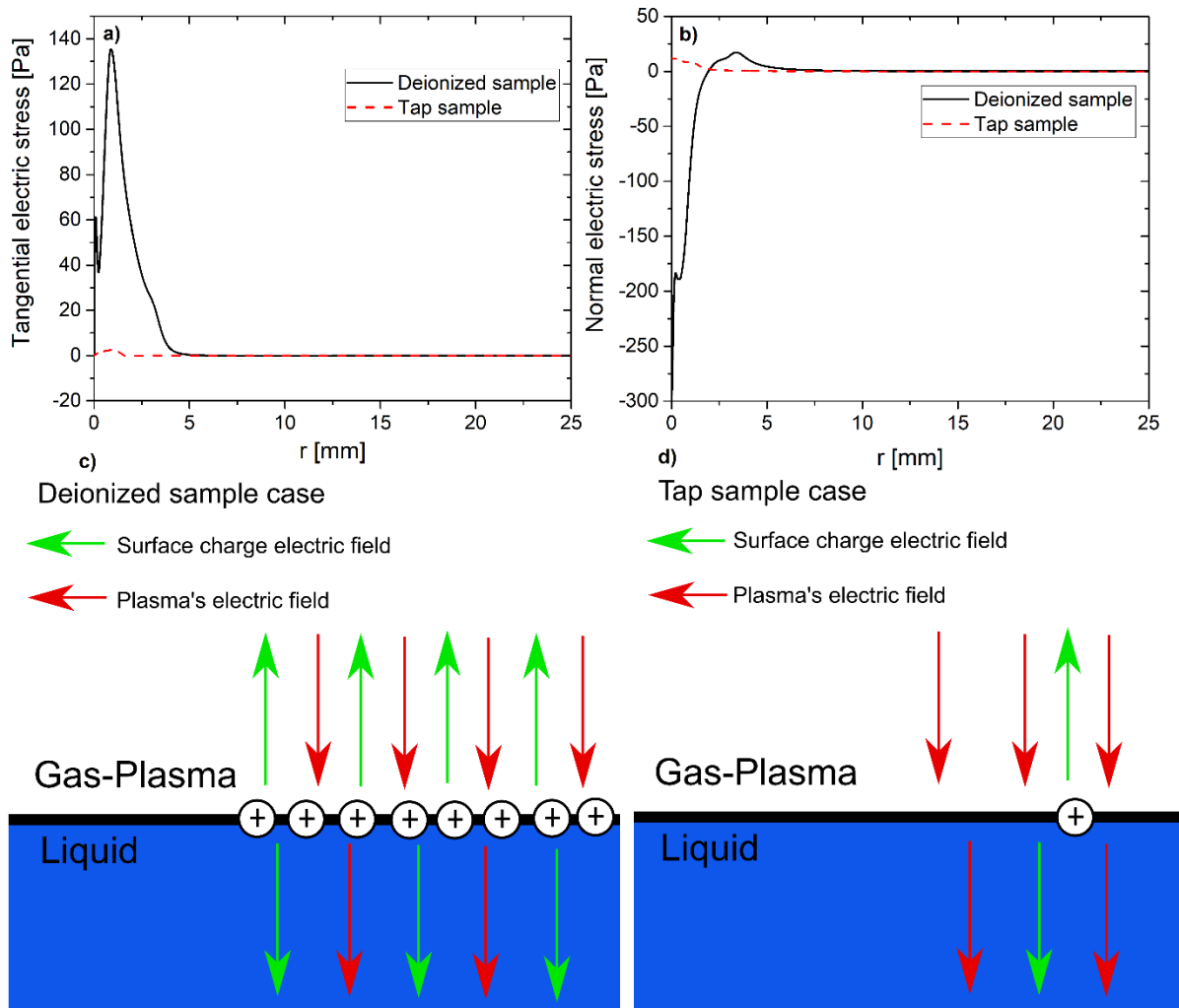


Figure 6: a) the time-averaged tangential electric surface stress for both investigated cases, b) the time-averaged normal electric surface stress for both investigated cases, c) a schematic showing the electric field strength at both sides of the interface for the deionized sample case, and d) a schematic showing the electric field strength at both sides of the interface for the tap sample case.

The tangential electric surface stress of the deionized sample is much larger than that of the tap sample case, as figure 6a shows. This stress is caused by the tangential electric field along the interface. As is known from electromagnetism, the tangential electric field of a perfect conductor is

zero⁵¹. Considering that the tap sample has a significantly higher conductivity than the deionized sample, the resultant tangential electric field was much lower, in the order of $1 \text{ kV}\cdot\text{cm}^{-1}$ at its maximum. In contrast, the tangential electric field in the deionized sample was on the order of $10 \text{ kV}\cdot\text{cm}^{-1}$ at its maximum, which led to larger tangential electric surface stress at the interface. For the normal electric surface stress, the explanation of the differences between the two cases comes from the deposited surface charge on the interface. As explained in section 4.2, the deionized sample maintained the surface charge for a longer time due to its lower conductivity. The accumulated surface charge on the interface weakened the electric field in the plasma side of the interface. On the liquid side, however, the electric field was enhanced due to the presence of the surface charge, as highlighted in figure 6c. Considering that the electric stress is a function of the square of electric field, the intensified electric field in the liquid medium on the order of $20 \text{ kV}\cdot\text{cm}^{-1}$ at its maximum, caused the electric stress in the liquid to be comparable to that in the plasma, which was on the order of $60 \text{ kV}\cdot\text{cm}^{-1}$ at its maximum. Since the dielectric constant of water is 81 times that of air, the normal electric stress shown in figure 6b had a negative jump as when moving from the liquid phase to the plasma phase. For the tap water, the accumulation of the surface charge was small thus the electric field in the plasma side of the interface was stronger than that in the liquid side, as shown in figure 6d, which was less than $0.05 \text{ kV}\cdot\text{cm}^{-1}$ at its maximum. This led to a positive jump when moving from the liquid phase into the plasma phase. These observations explain the difference in the polarity between the deionized and tap water samples, it also explains the difference in the amplitude of electric surface stresses between the deionized sample and the tap sample. Finally, considering that the water behaved as a dielectric in the deionized sample case, the plasma extended over a larger area in comparison to the tap sample, which led to the electric field stress for the deionized case to extend over a larger area than that of the tap sample case.

4.5 Plasma induced flow

After the EHD force fields and electric surface stresses on the interface were computed by the electric component of the model, they were used as input to the mechanical component to account

for the plasma-induced flow, which was solved until the flow arrived to a steady state. This allowed for the comparison of the model predicted flow field to that of the time-averaged PIV measurements. Figure 7 shows a comparison between the computed and measured velocity magnitude in the air and water regions, respectively. A reasonable agreement between the computed and measured flow fields can be observed. As can be seen in figure 7a, there is a gap in the measured data extending from the pin tip to the liquid surface. Unfortunately, this is an unavoidable consequence of the plasma emission masking scattered laser light from the seeding particles, making it impossible to calculate the velocity vectors within the most intense parts of the discharge. Figure 7 also shows that the air flow in the computed and the measured cases eventually go up, with the transition point occurring at a closer distance to the plasma in the measurement. This is a result of the higher temperature of the flowing gas in comparison to the ambient air, which sets buoyancy in action when the flow velocity is low, which was not taken into consideration in the model.

Figure 7 also indicates that the computed velocity magnitude in the liquid phase is slightly higher than the measured profile, despite having a similar structure. Considering that the model is deterministic and based on time-averaged force fields, it was unable to capture some of the flow instabilities observed experimentally on plasma-liquid interfaces³⁷. The absence of such instabilities meant that momentum transfer across the surface was overestimated, which led to higher velocity in the liquid phase.

In the gas phase, the EHD axial force induced a “jet” flow directed toward the liquid surface, with an average velocity in the region between the pin electrode and the interface of 1.5 ms^{-1} . The jet flow impinged on the surface and turned into a radial flow parallel to it. The radial EHD force in the contact area gives a further push to the radial flow. The radial gas flow dragged the interface through viscous stress coupling across the surface, which induced a shear flow in the bulk liquid on the order of 12 mm s^{-1} . The direction of the radial flow in the liquid phase was parallel to that in the

gas phase. The induced axial flow in the liquid phase was directed in the positive z direction in the order of 15 mm s^{-1} , transporting liquid from the bulk to the surface to provide the mass flow to support the radial flow at the surface. Comparing figure 7 to figure 3 it becomes evident that the shear flow in the liquid phase is dominated by the gas flow after breakdown, in comparison to electric surface stresses before breakdown. The contribution of the electric surface stresses after breakdown on the surface to the overall flow was found to be insignificant in the tap sample case. This was inferred by comparing the solution of the model when both mechanisms (EHD flow and electric surface stresses) are accounted for, to the solution when the EHD flow only is taken into account. The liquid flow was found to be less than 10% different between the two cases.

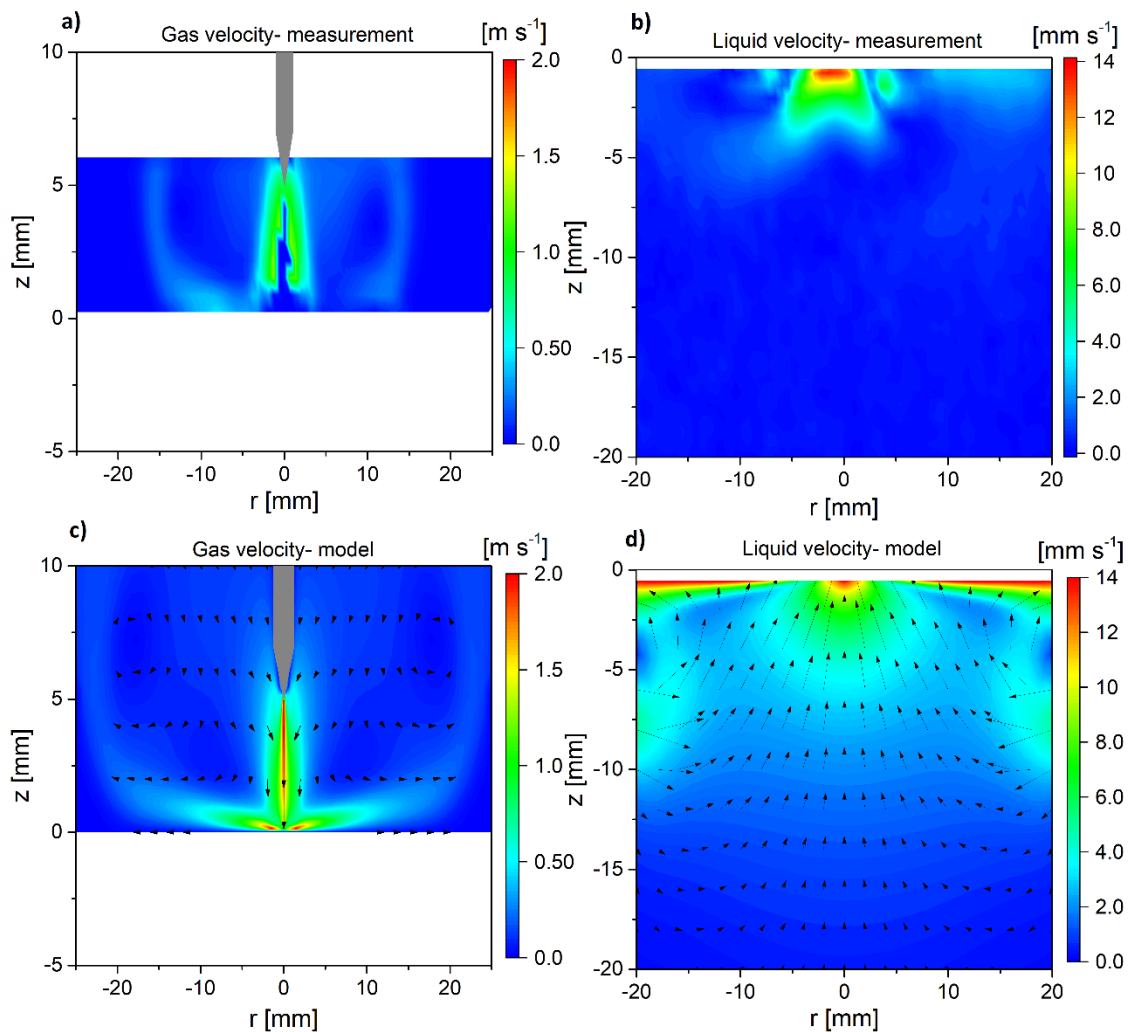


Figure 7: a) The magnitude of the measured gas velocity, b) the magnitude of the measured liquid velocity, c) the magnitude of the computed gas velocity, and d) the magnitude of the computed liquid velocity. All measured fields are shown for the tap sample case. Panels a and c have the same scale, panels c and d have the same scale. The white space in panels c and d indicate a region where it was not possible to obtain stable measurement of the flow.

With respect to the deionized sample case, despite absence of PIV data, the computed EHD forces and the electric surface stresses were input to the mechanical component to quantify their contribution to the predicted flow. The model showed that when both mechanisms were considered, the surface experienced large deformations and became unstable, which was consistent with the experimental observations. When the model was solved with EHD flow only, the liquid phase was stable and the deformation of the surface was minimal. To quantify this effect, the model was solved using the EHD force only until steady state flow in the liquid phase was established. At time 0, the electric surface stress was “switched on”. Figure 8 shows the deformation of the surface and the axial velocity on the symmetry axis over the first millisecond of switching on the electric surface stress. In this scenario, data was only captured over a short operating period as the large deformation of the interface required the electric component of the model to be updated to account for the new interface structure.

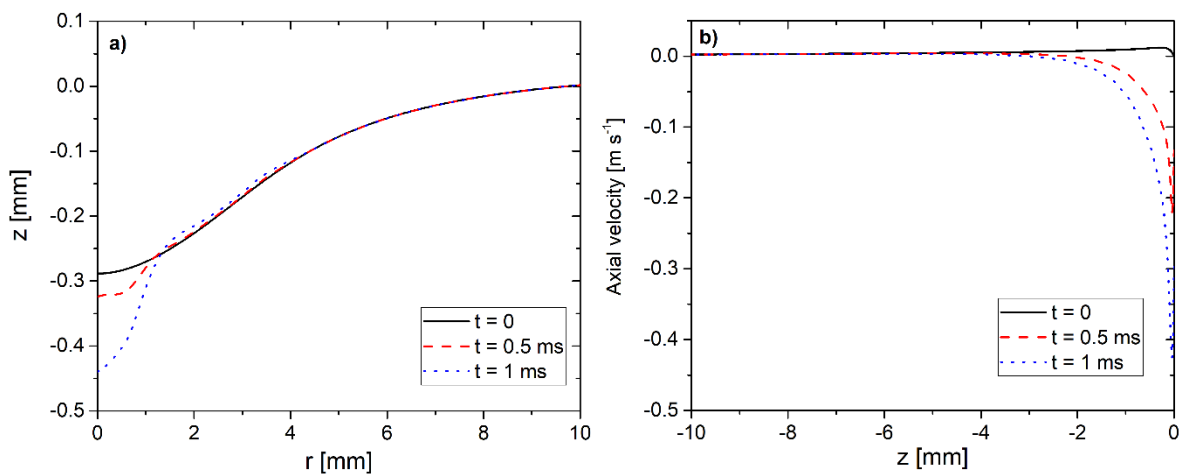


Figure 8: a) The surface displacement as a function of time after the electric surface stress was activated, $z = 0$ mm represents the position of the undistributed flat surface, $z = -0.3$ mm represents the steady state position of the surface perturbed by EHD forces alone, and b) the axial velocity in the liquid phase along the symmetry axis up until 1 ms after the electric surface stress was switched on. Both panels show the deionized case.

Negative values of z in panel b indicate the depth in the liquid phase.

Figure 8 indicates that the electric surface stresses dominated the liquid flow in the deionized water case, and that it is driving the instabilities at the interface in the first minutes of plasma generation. The surface instabilities cause the flow to become highly turbulent at the interface. Considering that the Sherwood number, which is a dimensionless parameter describing the rate of mass transfer across an interface, increases as the Reynolds number increases; a turbulent interface leads to a larger mass transfer rate across the interface, which would result in a faster activation of the treated liquid⁵².

It was observed experimentally that longer plasma exposures led to an increasingly stable flow in the liquid phase. This may be explained by considering the conductivity of the liquid, which is known to gradually increase during plasma exposure due to the increase of NO_2^- and NO_3^- in the liquid⁴². This acts to transform the liquid from a leaky dielectric into a poor conductor, thus the deionized water sample becomes more like the tap water case.

5. Conclusions

A two-dimensional axisymmetric model was developed to describe the mechanical interaction between the plasma and the treated liquid in a pin-water electrode system. The model solved for the plasma parameters, the flow fields in the gas and the liquid phase, and the deformation of the surface. Particle Image Velocimetry measurements were used to capture the velocity flow field in both the gas and the liquid, providing data to validate the computational model. A close agreement was observed between the model's predictions and the experimental measurements. The model

was solved for two water different samples: a deionized sample with a low conductivity of $2 \mu\text{S cm}^{-1}$ and a tap sample, which had a conductivity of $300 \mu\text{S cm}^{-1}$.

The model was used to investigate two mechanisms that contribute to driving the liquid flow, those were the EHD-induced flow in the background gas and the electric surface stresses across the interface. The time-averaged EHD force field was analysed and it was reported that the primary difference between the two investigated cases was in the axial component at the plasma-liquid contact area, where the force for the tap sample case was significantly larger than that of the deionized case. This was attributed to the strong electric field being maintained in the sheath for most of the applied period of the waveform as a result of the short lifetime of the surface charge on the interface. The electric surface stresses were shown to be an order of magnitude larger for the deionized sample in comparison to that of the tap sample. This was explained by the presence of the longer lifetime of the surface charge on the interface, which weakened the electric field in the air side of the plasma side of the interface and strengthened the electric field in the liquid side, leading to larger electric surface stresses.

The influence of the two mechanism on the liquid flow was investigated. It was shown that the electric surface stresses played a minimal role in the tap sample case, while in the deionized sample case they were responsible for large deformation of the interface, which significantly affected the liquid flow. These findings indicate that the electric stresses are the dominant mechanism driving the liquid flow when the liquid behaves as a dielectric, while the EHD-induced gas flow is the dominant mechanism driving the liquid flow when the liquid behaves as a conductor.

The large surface deformations reported for the deionized sample case led to strong turbulence at the interface. Considering that the mass transport rate across an interface is proportional to the Reynolds number, the findings of this study imply that the plasma activation of a liquid with a low conductivity occurs as a higher rate than those with a lower conductivity, leading to faster activation of the treated liquid.

Supplementary material

A video recording of the water's interface is included as supplementary material to show the instability at the interface arising when plasma treating the deionized water sample as described in the manuscript.

Acknowledgments

The authors JLW and MIH would like to acknowledge the support of ESPRC grants number EP/S025790/1, EP/N021347/1, and EP/T000104/1 for their support.

Data Availability

The data that support the findings of this study are available from the corresponding author upon reasonable request.

References

1. Attri, P., Ishikawa, K., Okumura, T., Koga, K. & Shiratani, M. Plasma agriculture from laboratory to farm: A review. *Processes* **8**, (2020).
2. Pan, Y., Cheng, J. H. & Sun, D. W. Cold Plasma-Mediated Treatments for Shelf Life Extension of Fresh Produce: A Review of Recent Research Developments. *Compr. Rev. Food Sci. Food Saf.* **18**, 1312–1326 (2019).
3. Martines, E. Interaction of cold atmospheric plasmas with cell membranes in plasma medicine studies. *Jpn. J. Appl. Phys.* **59**, (2020).
4. Mirpour, S. *et al.* Cold atmospheric plasma as an effective method to treat diabetic foot ulcers: A randomized clinical trial. *Sci. Rep.* **10**, 1–9 (2020).
5. Weltmann, K. D. & Von Woedtke, T. Plasma medicine - Current state of research and medical application. *Plasma Phys. Control. Fusion* **59**, (2017).
6. Williams, D. F., Kellar, E. J. C., Jesson, D. A. & Watts, J. F. Surface analysis of 316 stainless steel treated with cold atmospheric plasma. *Appl. Surf. Sci.* **403**, 240–247 (2017).

7. Wang, M. *et al.* Cold atmospheric plasma (CAP) surface nanomodified 3D printed polylactic acid (PLA) scaffolds for bone regeneration. *Acta Biomater.* **46**, 256–265 (2016).
8. Traylor, M. J. *et al.* Long-term antibacterial efficacy of air plasma-activated water. *J. Phys. D. Appl. Phys.* **44**, 1–5 (2011).
9. Kostya (ken) Ostrikov *et al.* Plasma-activated water: Generation, origin of reactive species and biological applications. *J. Phys. D. Appl. Phys.* **53**, (2020).
10. Vlad, I. E. & Anghel, S. D. Time stability of water activated by different on-liquid atmospheric pressure plasmas. *J. Electrostat.* **87**, 284–292 (2017).
11. Liu, D. X. *et al.* Aqueous reactive species induced by a surface air discharge: Heterogeneous mass transfer and liquid chemistry pathways. *Sci. Rep.* **6**, 1–11 (2016).
12. Verlackt, C. C. W., Van Boxem, W. & Bogaerts, A. Transport and accumulation of plasma generated species in aqueous solution. *Phys. Chem. Chem. Phys.* **20**, 6845–6859 (2018).
13. Tschang, C. Y. T. & Thoma, M. In vitro comparison of direct plasma treatment and plasma activated water on *Escherichia coli* using a surface micro-discharge. *J. Phys. D. Appl. Phys.* **53**, (2020).
14. Pawlat, J. *et al.* Evaluation of Oxidative Species in Gaseous and Liquid Phase Generated by Mini-Gliding Arc Discharge. *Plasma Chem. Plasma Process.* **39**, 627–642 (2019).
15. Du, C. M. *et al.* Erratum: The application of a non-thermal plasma generated by gas-liquid gliding arc discharge in sterilization (New Journal of Physics (2012) 14 (013010)). *New J. Phys.* **14**, (2012).
16. Tani, A., Ono, Y., Fukui, S., Ikawa, S. & Kitano, K. Free radicals induced in aqueous solution by non-contact atmospheric-pressure cold plasma. *Appl. Phys. Lett.* **100**, (2012).
17. Dobrynin, D., Fridman, G., Friedman, G. & Fridman, A. Physical and biological mechanisms of

- direct plasma interaction with living tissue. *New J. Phys.* **11**, (2009).
18. Hensel, K. *et al.* Effects of air transient spark discharge and helium plasma jet on water, bacteria, cells, and biomolecules. *Biointerphases* **10**, 029515 (2015).
 19. Diamond, J., Profili, J. & Hamdan, A. Characterization of Various Air Plasma Discharge Modes in Contact with Water and Their Effect on the Degradation of Reactive Dyes. *Plasma Chem. Plasma Process.* **39**, 1483–1498 (2019).
 20. Yoon, S. Y. *et al.* Mutual Interaction between Plasma Characteristics and Liquid Properties in AC-driven Pin-to-Liquid Discharge. *Sci. Rep.* **8**, 4–13 (2018).
 21. Krupež, J. *et al.* Degradation of nicotine in water solutions using a water falling film DBD plasma reactor: Direct and indirect treatment. *J. Phys. D. Appl. Phys.* **51**, (2018).
 22. Ito, T., Uchida, G., Nakajima, A., Takenaka, K. & Setsuhara, Y. Control of reactive oxygen and nitrogen species production in liquid by nonthermal plasma jet with controlled surrounding gas. *Jpn. J. Appl. Phys.* **56**, (2017).
 23. Bruggeman, P. J. *et al.* Plasma-liquid interactions: A review and roadmap. *Plasma Sources Sci. Technol.* **25**, (2016).
 24. Semenov, I. L., Weltmann, K. D. & Loffhagen, D. Modelling of the transport phenomena for an atmospheric-pressure plasma jet in contact with liquid. *J. Phys. D. Appl. Phys.* **52**, (2019).
 25. Van Rens, J. F. M. *et al.* Induced liquid phase flow by RF Ar cold atmospheric pressure plasma jet. *IEEE Trans. Plasma Sci.* **42**, 2622–2623 (2014).
 26. Park, S., Cvelbar, U., Choe, W. & Moon, S. Y. The creation of electric wind due to the electrohydrodynamic force. *Nat. Commun.* **9**, 371 (2018).
 27. Boeuf, J. P. & Pitchford, L. C. Electrohydrodynamic force and aerodynamic flow acceleration in surface dielectric barrier discharge. *J. Appl. Phys.* **97**, (2005).

28. Bruggeman, P., Graham, L., Degroote, J., Vierendeels, J. & Leys, C. Water surface deformation in strong electrical fields and its influence on electrical breakdown in a metal pin-water electrode system. *J. Phys. D. Appl. Phys.* **40**, 4779–4786 (2007).
29. Xie, J., Jiang, J., Davoodi, P., Srinivasan, M. P. & Wang, C. H. Electrohydrodynamic atomization: A two-decade effort to produce and process micro-/nanoparticulate materials. *Chem. Eng. Sci.* **125**, 32–57 (2015).
30. Hayati, I., Bailey, A. I. & Tadros, T. F. Mechanism of stable jet formation in electrohydrodynamic atomization. *Nature* **319**, 41–43 (1986).
31. Morad, M. R., Rajabi, A., Razavi, M. & Pejman Sereshkeh, S. R. A Very Stable High Throughput Taylor Cone-jet in Electrohydrodynamics. *Sci. Rep.* **6**, 1–10 (2016).
32. Wang, Z., Xia, L. & Zhan, S. Experimental study on electrohydrodynamics (EHD) spraying of ethanol with double-capillary. *Appl. Therm. Eng.* **120**, 474–483 (2017).
33. Collins, R. T., Jones, J. J., Harris, M. T. & Basaran, O. A. Electrohydrodynamic tip streaming and emission of charged drops from liquidcones. *Nat. Phys.* **4**, 149–154 (2008).
34. Das, D. & Saintillan, D. Electrohydrodynamics of viscous drops in strong electric fields: Numerical simulations. *J. Fluid Mech.* **829**, 127–152 (2017).
35. Zehtabiyani-Rezaie, N., Saffar-Avval, M. & Adamiak, K. Numerical investigation of water surface deformation due to corona discharge. *J. Electrostat.* **96**, 151–159 (2018).
36. Mitsugi, F., Kusumegi, S., Nishida, K. & Kawasaki, T. Visualization of Plasma-Induced Liquid Flow Using KI-Starch and PIV. *IEEE Trans. Plasma Sci.* **49**, 1–6 (2020).
37. Lai, J., Petrov, V. & Foster, J. E. Understanding Plasma-Liquid Interface Instabilities Using Particle Image Velocimetry and Shadowgraphy Imaging Methods. *IEEE Trans. Plasma Sci.* **46**, 875–881 (2018).

38. Raffel, M., Willert, C. E., Wereley, S. & Kompenhans, J. Particle Image Velocity A Practical Guide. in (ed. Springer) 15–77 (2012).
39. Morabit, Y., Whalley, R. D., Robert, E., Hasan, M. I. & Walsh, J. L. Turbulence and entrainment in an atmospheric pressure dielectric barrier plasma jet. *Plasma Process. Polym.* **17**, 1–12 (2020).
40. Whalley, R. D. & Walsh, J. L. Turbulent jet flow generated downstream of a low temperature dielectric barrier atmospheric pressure plasma device. *Sci. Rep.* **6**, 1–7 (2016).
41. Tropea, C., Yarin, A. & Foss, J. *Springer Handbook of Experimental Fluid Mechanics*. (2007). doi:10.2514/1.38773.
42. Judée, F., Simon, S., Bailly, C. & Dufour, T. Plasma-activation of tap water using DBD for agronomy applications: Identification and quantification of long lifetime chemical species and production/consumption mechanisms. *Water Res.* **133**, 47–59 (2018).
43. Vanderlinde, J. Classical Electromagnetic Theory. in 69–92 (Springer, 2005).
44. Zienkiewicz, O., Taylor, R. & Nithiarasu, P. The Finite Element Method for Fluid Dynamics. in *Elsevier* (2005).
45. Sakiyama, Y., Graves, D. B., Chang, H. W., Shimizu, T. & Morfill, G. E. Plasma chemistry model of surface microdischarge in humid air and dynamics of reactive neutral species. *J. Phys. D. Appl. Phys.* **45**, (2012).
46. MORGAN database. www.lxcat.net (2016).
47. Hagelaar, G. J. M. & Pitchford, L. C. Solving the Boltzmann equation to obtain electron transport coefficients and rate coefficients for fluid models. *Plasma Sources Sci. Technol.* **14**, 722–733 (2005).
48. Diamond, J., Hamdan, A., Profili, J. & Margot, J. Time and space-resolved imaging of an AC air

- discharge in contact with water. *J. Phys. D. Appl. Phys.* **53**, (2020).
49. Sun, L., Huang, X., Zhang, J., Zhang, J. & Shi, J. J. Discharge dynamics of pin-to-plate dielectric barrier discharge at atmospheric pressure. *Phys. Plasmas* **17**, 1–5 (2010).
 50. Lu, X. P. & Laroussi, M. Ignition phase and steady-state structures of a non-thermal air plasma. *J. Phys. D. Appl. Phys.* **36**, 661–665 (2003).
 51. Jackson, J. D. Classical Electrodynamics. in (John Wiley and sons, 1999).
 52. Colombet, D., Legendre, D., Cockx, A. & Guiraud, P. Mass or heat transfer inside a spherical gas bubble at low to moderate Reynolds number. *Int. J. Heat Mass Transf.* **67**, 1096–1105 (2013).